

# ChemComm

Accepted Manuscript



This is an *Accepted Manuscript*, which has been through the Royal Society of Chemistry peer review process and has been accepted for publication.

*Accepted Manuscripts* are published online shortly after acceptance, before technical editing, formatting and proof reading. Using this free service, authors can make their results available to the community, in citable form, before we publish the edited article. We will replace this *Accepted Manuscript* with the edited and formatted *Advance Article* as soon as it is available.

You can find more information about *Accepted Manuscripts* in the [Information for Authors](#).

Please note that technical editing may introduce minor changes to the text and/or graphics, which may alter content. The journal's standard [Terms & Conditions](#) and the [Ethical guidelines](#) still apply. In no event shall the Royal Society of Chemistry be held responsible for any errors or omissions in this *Accepted Manuscript* or any consequences arising from the use of any information it contains.



## Chemical Communication

## COMMUNICATION

## Turning conductive carbon nanospheres to nanosheets for high-performance supercapacitors of MnO<sub>2</sub> nanorods

Received 00th January 20xx,  
Accepted 00th January 20xx

DOI: 10.1039/x0xx00000x

www.rsc.org/

Nuttaphon Phattharasupakun,<sup>a</sup> Juthaporn Wutthiprom,<sup>a</sup> Poramane Chiochan,<sup>a</sup> Phansiri Suktha,<sup>a</sup> Montakan Suksomboon,<sup>a</sup> Saran Kalasina,<sup>a</sup> and Montree Sawangphruk<sup>a\*</sup>

The oxidized carbon nanosheets (OCN), produced from black carbon nanospheres and used as a conductive additive in the supercapacitor electrodes of MnO<sub>2</sub> nanorods, can significantly improve the charge-storage performance of the symmetric MnO<sub>2</sub>-nanorod supercapacitors with a maximum specific energy of 64 Wh/kg and power of 3870 W/kg. An optimum material composition of the supercapacitor electrode finely tuned is 60:30:10 wt.% of MnO<sub>2</sub>:OCN:PVDF, respectively. Interestingly, after 5000 charge/discharge cycles, the oxidation numbers of Mn at the positive and negative electrodes of the as-fabricated supercapacitor are +3.22 and +3.04, respectively.

Supercapacitors provide higher specific power (~500-10,000 W/kg) with faster charge/discharge rates and longer cycle life (>100,000 cycles) when compared with batteries<sup>1,2</sup>. Generally, the electrodes of the supercapacitors consist of three materials: (i) active materials storing electronic and ionic charges on their surfaces, (ii) conductive materials used to assist the electronic charge transport within the electrode and between the active materials and the current collectors or substrates during charging/discharging, and (iii) adhesive binders (i.e., PVDF) employed to hold the materials together on the substrate surfaces.

The supercapacitor materials can be classified by their charge storage mechanisms. Electrochemical double layer capacitance (EDLC) materials such as graphene, activated carbon, and carbon aerogel store ionic charges via a physical adsorption process on their conductive surfaces and porosities<sup>3</sup>. On the other hand, pseudocapacitance materials e.g., transition-metal oxides/hydroxides and conducting polymers store electronic charges via a surface redox reaction leading to high specific capacitance<sup>1,2</sup>. However, the pseudocapacitance metal oxides

and hydroxides have rather poor conductivity. Thus, the conductive additives such as black carbon nanospheres (CN) are typically used in the fabrication process of the supercapacitor electrodes.

Among various transition-metal oxides, MnO<sub>2</sub> has been widely studied due to its high theoretical specific capacitance (1233 F/g)<sup>4-6</sup>, low cost, natural abundance, and environmental compatibility. Previously, MnO<sub>2</sub> supercapacitors produced by an ultrasound-microwave-assisted method provided a specific capacitance (SC) of 214 F/g at 2 mA/cm<sup>2</sup><sup>7</sup>. Incorporation of MnO<sub>2</sub>-coated carbon nanotubes with graphene nanosheets exhibited a SC of 193 F/g at 0.2 A/g<sup>8</sup>. Nitrogen-doped graphene-ultrathin MnO<sub>2</sub> composites prepared by a hydrothermal method exhibited a SC of 257.1 F/g at 0.2 A/g<sup>9</sup>. Graphene-wrapped honeycomb MnO<sub>2</sub> nanospheres via an electrostatic interaction showed a SC of 210 F/g at 0.5 A/g<sup>10</sup>. 2D MnO<sub>2</sub>/graphene hybrid nanostructures provided a SC of 267 F/g at 0.2 A/g<sup>11</sup>. In this work, MnO<sub>2</sub> nanorods with high aspect ratio were used as the active material of the supercapacitors.

In addition, the conductive CN was chemically converted to carbon nanosheets by an oxidation process (see experimental detail in the supporting information) and used in the supercapacitor electrodes. Furthermore, we have investigated the effect of material compositions on the performance of the supercapacitors. From previous reports, the weight ratios of active material: conductive additive: adhesive additive were different leading to uncertainty in performance comparison of the supercapacitors. Among various ratios, a weight ratio of 80:10:10 wt.% was frequently used in the fabrication process of the supercapacitor electrodes<sup>12-15</sup>. To the best of our knowledge, no previous report explained why this ratio was employed. The results here in this work surprisingly showed that the oxidized carbon nanosheets (OCN) can significantly improve the charge storage performance of the supercapacitors. The optimum weight ratio of MnO<sub>2</sub>:OCN:

<sup>a</sup> Department of Chemical and Biomolecular Engineering, School of Energy Science and Engineering, Vidyasirimedhi Institute of Science and Technology, Rayong 21210, Thailand

\*Corresponding author. Tel: +66(0)33-01-4251 Fax: +66(0)33-01-4445. E-mail address: montree.s@vistec.ac.th (M. Sawangphruk).

† Footnotes relating to the title and/or authors should appear here.

Electronic Supplementary Information (ESI) available: Experimental and calculation details as well as FESEM and electrochemical results. See DOI: 10.1039/x0xx00000x

PVDF finely tuned is 60:30:10 wt.%, which is not the same ratio as the previous report<sup>12-15</sup>.

The morphology of CN characterized by a field emission-scanning electron microscope (FE-SEM) is shown in Fig. 1a for which the spherical morphology of the aggregated CN is observed. While, the FE-SEM image of OCN after the oxidation process in Fig. 1b shows a remarkable morphological change from nanospheres to nanosheets. An FE-SEM image of MnO<sub>2</sub> nanorods, marketed from Sigma-Aldrich and used as the active material, is also shown in Fig.S1 of the supporting information. The MnO<sub>2</sub> nanorods have an average diameter of ca. 20 nm with a high aspect ratio of ca. 20. Fig.1c shows a transmission electron microscope (TEM) image of CN, which reveals a spherical structure with a diameter of about 50 nm. The aggregated nanospheres form the branch structure leading to high electronic conductivity. After the oxidation process, a TEM image of OCN is shown in Fig.1d for which the morphology of the OCN is a sheet-like structure. An inset image in Fig. 1d shows an HRTEM of OCN for which the crystalline carbon particle has a distance between adjacent planes ca. 0.34 nm, which is comparable with the (002) d-spacing in graphitic carbon materials.

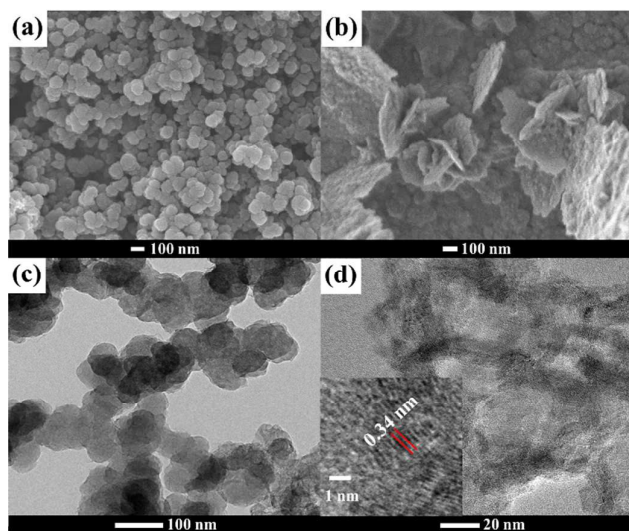


**Fig. 1.** FE-SEM images of (a) black carbon nanospheres (CN) and (b) oxidized CN (OCN) as well as TEM images of (c) CN and (d) OCN.

Raman spectra of CN and OCN shown in Fig.2a exhibit the characteristic peaks of the carbon-based materials. D band (disordered) at 1350 cm<sup>-1</sup> is due to the vibration mode of sp<sup>3</sup> carbon atoms chemically bonded to oxygen-containing groups and carbon at the edge of the graphitic sheets. Whilst, G band at 1580 cm<sup>-1</sup> represents the vibration of sp<sup>2</sup> graphitic carbon<sup>16</sup>. Both D and G bands of the OCN have higher intensity when compared with those of the CN since the oxidation process can also remove the amorphous phase of the CN, overall providing more crystalline phases in the OCN sample. The I<sub>D</sub>/I<sub>G</sub> ratios of CN and OCN are 1.233 and 1.273, respectively. This indicates that the OCN has more sp<sup>3</sup> carbon atoms due to the oxygen-containing functional groups on its surface. The lateral size (L<sub>a</sub>) values of the crystallites calculated from the Raman spectra<sup>17</sup> are 3.417 and 3.527 nm for CN and OCN, respectively. The FTIR spectra of CN and OCN in Fig.2b exhibit broad peaks at the

wavenumbers of 1350-1600 cm<sup>-1</sup> due to C-C and C-H stretching modes of the sp<sup>2</sup> carbon atoms and 3300-3500 cm<sup>-1</sup> due to O-H stretching vibrations from the moisture adsorbed. The OCN exhibits broad bands at 1200-1250 cm<sup>-1</sup> owing to C-O stretching vibrations of alcohol and carboxyl groups and at 1720-1740 cm<sup>-1</sup> due to C=O stretching vibrations of the carboxyl groups. These can be concluded that the oxidation process under a reflux condition (see more details in the supporting information) not only change the morphology of CN but also it generates the functional groups at the surface of OCN, which can eventually help improving the performance of supercapacitors due to its high ionic conductivity.

Fig. 2c shows the XRD patterns of CN and OCN for which two peaks at 2θ around 25° and 43° can be indexed to (002), and (100) plane directions, respectively showing the characteristics of graphitic carbon<sup>18, 19</sup>. Based on the (002) direction, the calculated stacking height (L<sub>c</sub>) values of the CN and OCN are 3.147 and 4.129 nm, respectively. This indicates that the expanded graphitic layers can be achieved by the oxidation process. N<sub>2</sub> adsorption/desorption measurements were employed to investigate the porous structure of CN and OCN shown in Fig.2d. Both materials have a type IV adsorption isotherm with H3 hysteresis loop according to the IUPAC classification, which is a characteristic of mesoporous carbon materials<sup>6, 20</sup>. The BET specific surface areas of CN and OCN are 119.7 and 186.1 m<sup>2</sup>/g, respectively. The increased surface area of OCN may lead to high charge-storage performance.

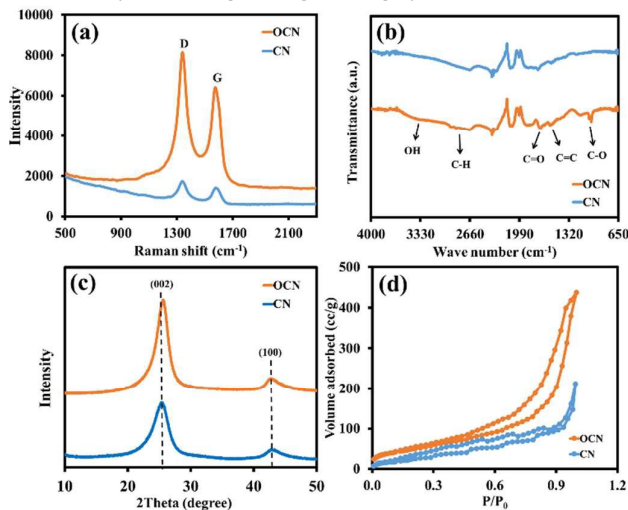


**Fig. 2.** (a) Raman spectra, (b) FT-IR spectra, (c) XRD patterns, and (d) N<sub>2</sub> sorption isotherms of CN and OCN.

To further evaluate the electrochemical properties of the CN and OCN, the MnO<sub>2</sub> nanorod supercapacitors using CN and OCN as the conductive additives were therefore fabricated and evaluated by cyclic voltammetry (CV), galvanostatic charge/discharge (GCD), and electrochemical impedance spectroscopy (EIS). Fig.3a shows the CV of the supercapacitors with a CR2016 size fabricated using different mass ratios of MnO<sub>2</sub>/OCN/PVDF. Note, the controlled experiment (8:1:1

MnO<sub>2</sub>/CN/PVDF) was also carried out for comparison. The CV was measured at a scan rate of 10 mV/s in a potential range of -0.5 to 2.0 V. It is clearly observed that the supercapacitor using 6:3:1 MnO<sub>2</sub>/OCN/PVDF exhibits the largest specific current, indicating the superior electrochemical performance of MnO<sub>2</sub>/OCN/PVDF coated on functionalized-carbon fibre paper (*f*-CFP)<sup>21</sup>. Note, the MnO<sub>2</sub>/OCN/PVDF supercapacitors here have much higher charge storage performance than the MnO<sub>2</sub>-based supercapacitors fabricated for comparison in this work using reduced graphene oxide (rGO) as the conductive additive (see Fig. S3). As shown in Fig.3b, the specific capacitances of the supercapacitors decrease as a function of the scan rates due to the diffusion limit<sup>22</sup>. At low scan rate, the ions have more time to diffuse from the electrolyte separator into accessible deep pores of the electrode leading to higher specific capacitance while at high scan rate, the ions are mainly adsorbed on the outer surface of the electrode<sup>6, 23</sup>. In addition, the MnO<sub>2</sub>-based supercapacitors using reduced graphene oxide as the conductive material were fabricated for comparison with OCN.

GCD in Fig.3c also shows the same tendency as the CV result. The calculated specific capacitances from the GCD results vs. the applied specific currents are shown in Fig. 3d. The MnO<sub>2</sub>/OCN/PVDF supercapacitor at a ratio of 6:3:1 has rather high specific capacitance of 414.28 F/g at 1 mA (0.35 A/g) when compared with others. The corresponding specific capacitances of MnO<sub>2</sub>/OCN/PVDF supercapacitors at other mass ratios of 9:0:1, 8.5:0.5:1, 8:1:1, 7:2:1, 5:4:1, and 4:5:1 and the MnO<sub>2</sub>/CN/PVDF supercapacitor at 8:1:1 are 179.36, 197.36, 273.40, 384.56, 261.56, 239.80, and 209.52 F/g at 1 mA, respectively. When compared to the 8:1:1 MnO<sub>2</sub>/CN/PVDF supercapacitor, the 6:3:1 MnO<sub>2</sub>/OCN/PVDF supercapacitor exhibits 1.65-fold higher specific capacitance. More interestingly, the as-fabricated supercapacitor in this work exhibits higher specific capacitance than the MnO<sub>2</sub>-based supercapacitors using different electrode material compositions (see Table S1 of the supporting information). This is because the -OH and -COOH functionalities of OCN can draw the ionic electrolytes to the electrodes<sup>24</sup>. The OCN with higher crystalline phase than CN has an ideal channel for the fast diffusion of electrolyte during charging/discharging. The specific capacitances decrease as a function of the applied currents for all as-fabricated supercapacitors in Fig. 3d owing to the diffusion limit.

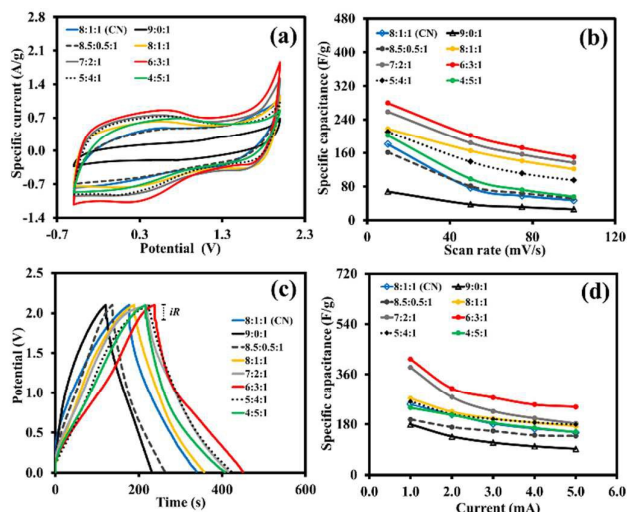


**Fig. 3.** (a) CVs at a scan rate of 10 mV/s, (b) the specific capacitances as a function of the scan rates, (c) GCDs at 2 mA and (d) the specific capacitances as a function of the applied currents of the MnO<sub>2</sub>:OCN:PVDF coated on *f*-CFP at different mass ratios.

The Nyquist plots of the MnO<sub>2</sub>/OCN/PVDF supercapacitors at different mass ratios exhibit straight line in the low-frequency region as shown in Fig.4a. The as-fabricated supercapacitor at 6:3:1 shows nearly vertical line close to the ideal capacitor. This supercapacitor also has the lowest ESR of 1.88 Ω when compared with others. The specific capacitance vs. applied frequency shown in Fig.4b indicates that at the lowest frequency (1 mHz), the 6:3:1 MnO<sub>2</sub>/OCN/PVDF supercapacitor exhibits the highest specific capacitance of 363.28 F/g. Fig.4c shows the Ragone plots of the MnO<sub>2</sub>/OCN/PVDF supercapacitors. The supercapacitor at 6:3:1 exhibits the highest specific energy (64.39 Wh/kg) and power (3870.01 W/kg). The capacity retention of the supercapacitor cells is also shown in Fig.4d. The as-fabricated supercapacitor at 6:3:1 has over 94% capacity retention after charged/discharged for 5000 cycles while that of the supercapacitor at 8:1:1 has only 84% capacity retention.

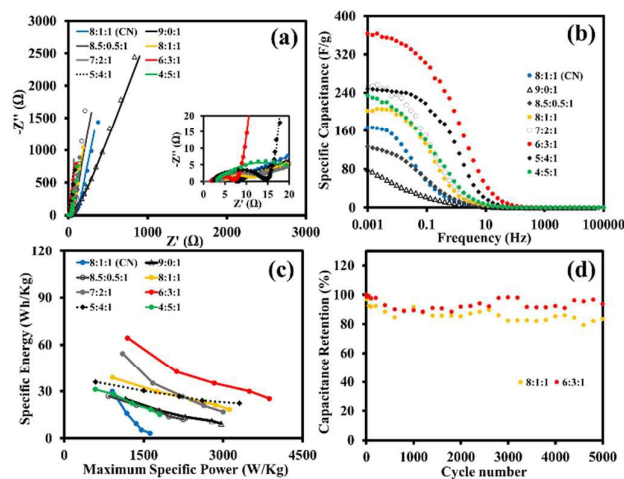


**Fig. 4.** (a) Nyquist plots, (b) specific capacitances vs. applied frequency plots, (c) Ragone plots, and (d) the capacitance retention over 5000 cycles of the  $\text{MnO}_2\text{:OCN:PVPDF}$  cells at 6:3:1 and 8:1:1.

To further evaluation of the oxidation number of manganese oxide used as the active materials in the supercapacitors, ex-situ high-resolution XAS of the supercapacitor electrodes was evaluated after the 5000<sup>th</sup> cycles. Basically, the starting material  $\text{MnO}_2$  nanorods have an oxidation number of +4. Interestingly, after the stability test over 5000 cycles, the oxidation numbers of the Mn in the positive and negative electrodes are +3.22 and +3.04, respectively. The difference here indicates that the electronic structure of  $\text{MnO}_2$  has changed after 5000 charge/discharge cycles.

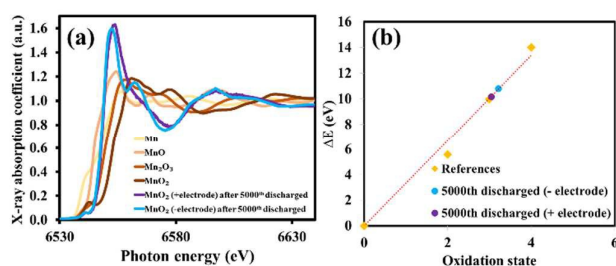


**Fig. 5.** Ex-situ high-resolution XAS spectra of the manganese oxide after the stability test over 5000 cycles compared with the Mn standard compounds.

In summary, conductive black carbon nanospheres (CNs) were successfully changed to nanosheets using an oxidation process leading to higher surface area and oxygen-containing groups on its surface. The atomic and crystalline structure of the oxidized CN characterized by HR-TEM, XRD, and RAMAN consists of  $\text{sp}^2$  graphitic carbon remaining high conductivity. The formulation ratio of active  $\text{MnO}_2$  material, conductive material, and PVDF binder was finely tuned and found that a 6:3:1 ratio of those materials is an optimum material composition raising the awareness in this research area that the electrode formulation plays a major role in controlling the performance of the as-fabricated supercapacitors. In addition, ex-situ XAS was eventually employed to investigate the oxidation number of Mn in the symmetric supercapacitor of 6:3:1  $\text{MnO}_2\text{:OCN:PVPDF}$  after the stability test over 5000 cycles. The oxidation numbers of Mn in the positive and negative electrodes of the supercapacitor are +3.22 and +3.04, respectively. This finding indicates that the electronic structure of  $\text{MnO}_2$  is changed after 5000 charge/discharge cycles.

## Notes and references

This work was financially supported by the Thailand Research Fund and Vidyasirimedhi Institute of Science and Technology (RSA5880043). Support from the Frontier Research Centre at VISTEC is also acknowledged.

1. P. Simon and Y. Gogotsi, *Nat. Mater.*, 2008, **7**, 845-854.
2. M. Winter and R. J. Brodd, *Chem. Rev.*, 2004, **104**, 4245-4270.
3. S. Mondal, U. Rana and S. Malik, *Chem. Commun.*, 2015, **51**, 12365-12368.
4. H. Wang, C. Peng, J. Zheng, F. Peng and H. Yu, *Mater. Res. Bull.*, 2013, **48**, 3389-3393.
5. S. J. Zhu, J. Q. Jia, T. Wang, D. Zhao, J. Yang, F. Dong, Z. G. Shang and Y. X. Zhang, *Chem. Commun.*, 2015, **51**, 14840-14843.
6. M. Sawangphruk, P. Srimuk, P. Chiochan, A. Krittayavathananon, S. Luanwuthi and J. Limtrakul, *Carbon*, 2013, **60**, 109-116.
7. P. Wang, Y.-J. Zhao, L.-X. Wen, J.-F. Chen and Z.-G. Lei, *Ind. Eng. Chem. Res.*, 2014, **53**, 20116-20123.
8. Z. Lei, F. Shi and L. Lu, *ACS appl. mater. interfaces*, 2012, **4**, 1058-1064.
9. S. Yang, X. Song, P. Zhang and L. Gao, *ACS appl. mater. interfaces*, 2013, **5**, 3317-3322.
10. J. Zhu and J. He, *ACS appl. mater. interfaces*, 2012, **4**, 1770-1776.
11. L. Peng, X. Peng, B. Liu, C. Wu, Y. Xie and G. Yu, *Nano Lett.*, 2013, **13**, 2151-2157.
12. R. Liu, E. Liu, R. Ding, K. Liu, Y. Teng, Z. Luo, Z. Li, T. Hu and T. Liu, *Ceram. Int.*, 2015, **41**, 12734-12741.
13. Y. Cao, Y. Xiao, Y. Gong, C. Wang and F. Li, *Electrochim. Acta*, 2014, **127**, 200-207.
14. W. Yao, H. Zhou and Y. Lu, *J. Power Sources*, 2013, **241**, 359-366.
15. L. Ma, X. Shen, Z. Ji, G. Zhu and H. Zhou, *Chem. Eng. J.*, 2014, **252**, 95-103.
16. A. C. Ferrari, *Solid State Commun.*, 2007, **143**, 47-57.
17. T. Ungár, J. Gubicza, G. Ribárik, C. Pantea and T. W. Zerdá, *Carbon*, 2002, **40**, 929-937.
18. H. Wang, Z. Xu, Z. Li, K. Cui, J. Ding, A. Kohandehghan, X. Tan, B. Zahiri, B. C. Olsen, C. M. Holt and D. Mitlin, *Nano Lett.*, 2014, **14**, 1987-1994.
19. A. K. Mondal, B. Wang, D. Su, Y. Wang, S. Chen, X. Zhang and G. Wang, *Mater. Chem. Phys.*, 2014, **143**, 740-746.
20. B. Zhao, H. Zhuang, T. Fang, Z. Jiao, R. Liu, X. Ling, B. Lu and Y. Jiang, *J. Alloy. Comp.*, 2014, **597**, 291-298.
21. P. Suktha, P. Chiochan, P. Iamprasertkun, J. Wutthiprom, N. Phattharasupakun, M. Suksomboon, T. Kaewsongpol, P. Sirisinudomkit, T. Pettong and M. Sawangphruk, *Electrochim. Acta*, 2015, **176**, 504-513.
22. J. Yan, Z. Fan, T. Wei, W. Qian, M. Zhang and F. Wei, *Carbon*, 2010, **48**, 3825-3833.
23. M. Sawangphruk, M. Suksomboon, K. Kongsupornsak, J. Khuntilo, P. Srimuk, Y. Sanguansak, P. Klunbud, P. Suktha and P. Chiochan, *J. Mater. Chem. A*, 2013, **1**, 9630-9636.
24. Y. Hou, Y. Cheng, T. Hobson and J. Liu, *Nano Lett.*, 2010, **10**, 2727-2733.